Journal of Materials Chemistry A

ROYAL SOCIETY OF CHEMISTRY

PAPER

View Article Online
View Journal

Cite this: DOI: 10.1039/d2ta09871g

Enhancing thermoelectric performance *via* relaxed spin polarization upon magnetic impurity doping†

Min Young Kim, ‡[a] Dongwook Kim, ‡[b] Gwansik Kim,[c] Wooyoung Lee, [cd] Nicolas Perez,[e] Kornelius Nielsch,[efg] Ji Hoon Shim*[bh] and Hyungyu Jin *[ai]

Developing a new strategy to mitigate the trade-off between the Seebeck coefficient, electrical conductivity, and thermal conductivity is of great importance for designing highly efficient thermoelectric (TE) materials. Recently, utilizing magnetism or spin degree-of-freedom has attracted interest as an effective way to overcome such a trade-off. Here, an unprecedented pathway to enhance the Seebeck coefficient is proposed in a magnetic-impurity-doped half metal by virtue of a novel "spin polarization relaxation" mechanism. Using Fe/Co-doped higher-manganese silicides (HMSs) as a platform, it is shown that alteration of the magnetic structure and accompanying modification of the spin-dependent band structure can lead to a significantly improved Seebeck coefficient. Magnetic characterization suggests that extrinsic Fe/Co ions are antiferromagnetically coupled with intrinsic Mn ions, reducing the magnetic moment of the doped HMS. Spin-polarized density functional theory calculations disclose that such antiferromagnetic coupling leads to magnetization-induced band shifts and thus the relaxed spin polarization of density-of-states at the Fermi level. Based on those calculation results, a two-spin-channel transport model is developed to explain the relationship between the relaxed spin polarization and the drastic increase of the Seebeck coefficient in the doped HMS. Our study opens up new TE research opportunities in various spin-polarized systems such as half metals which have seldom been investigated so far.

Received 19th December 2022
Accepted 12th April 2023

DOI: 10.1039/d2ta09871g

rsc.li/materials-a

Introduction

The climate crisis is now omnipresent around the world and weaving through our daily lives. The climate changes are triggered by the intensifying global warming due to carbon emissions in various energy conversion processes and give rise to extreme weather events including heavy rainfall, droughts and abnormal high temperatures nowadays. As a result, global voices now call for fossil fuel divestment and thus the importance of carbon-neutral technologies is growing day by day. Energy-harvesting is a representative of carbon-neutral technologies in that it can convert ambient energy present in the environment into electrical energy for use, and such a characteristic establishes itself as a next-generation technology. In particular, thermoelectric (TE) power generation based on the Seebeck effect has been the subject of much research over the past few decades now that it enables heat-to-electricity conversion from omnipresent waste heat.

The TE power generation could be practically applicable with integration devices composed of many pairs of TE elements including p- and n-type semiconductors. In here, the TE efficiency of the devices is largely determined by material characteristics of the elements, and thus, it is indispensable to enhance the TE performance of the material itself to increase the device TE efficiency ultimately. For instance, the efficiency of the Seebeck devices primarily relies on the material's TE properties such as the thermal conductivity κ, the Seebeck coefficient S, and the electrical conductivity σ, and thus the dimensionless figure-of-merit $zT = \frac{S^2\sigma}{\kappa}T$ (T: absolute temperature) eventually evaluates a material's TE efficiency. So, it has been emphasized that S and σ should be increased, and κ decreased to maximize zT.

[a]Department of Mechanical Engineering, Pohang University of Science and Technology (POSTECH), Pohang, 37673, South Korea. E-mail: hgjin@postech.ac.kr
[b]Department of Chemistry, Pohang University of Science and Technology (POSTECH), Pohang, 37673, South Korea. E-mail: jhshim@postech.ac.kr
[c]Department of Material Science and Engineering, Yonsei University, Seoul, 03722, South Korea
[d]Affiliate Faculty, Materials Research Center for Batteries, Pohang University of Science and Technology (POSTECH), Pohang, 37673, South Korea
[e]Leibniz Institute for Solid State and Materials Science, Dresden, 01069, Germany
[f]Institute of Materials Science, TU Dresden, Dresden, 01062, Germany
[g]Institute of Applied Physics, TU Dresden, Dresden, 01062, Germany
[h]Division of Advanced Materials Science, Pohang University of Science and Technology (POSTECH), Pohang, 37673, South Korea
[i]Institute for Convergence Research and Education in Advanced Technology, Yonsei University, Seoul, 03722, South Korea

† Electronic supplementary information (ESI) available. See DOI: https://doi.org/10.1039/d2ta09871g

‡ These authors contributed equally to this work.

Over the past few years, many strategies have been proposed to develop a high zT TE material,[1–4] among which a phonon-glass electron-crystal approach[5] has been the most favored method; selective scattering of phonons and electrons allows reduced κ and advanced $S^2\sigma$ for maximizing zT. In detail, "phonon-glass" hinders the phonon transport in materials like in glass with correspondingly decreasing lattice contribution to κ, while "electron-crystal" is responsible for efficient charge transport like in a crystal resulting in the retention of high S and σ within the same material. This approach can be effectively implemented with nanostructuring[6] and until now has been producing many remarkable results in TE materials research.[1–4]

Meanwhile, there is a new wave of interest in "spin thermoelectrics" where magnetic moments or spin degree-of-freedom of solids, seldom considered in conventional TE research, are actively utilized to improve TE properties. This strategy has been successfully demonstrated in various TE materials by embedding magnetic impurities.[7–15] Such magnetic impurities are shown to strengthen both phonon scattering and electron scattering for lower κ and a higher power factor ($=S^2\sigma$) in a way of overcoming the conflicts among the TE properties. Especially, the large enhancement in S has been attributed to spin-induced additional scattering of charge electrons. To mention several examples from the literature, an inclusion of superparamagnetic Co-nanoparticles (NPs) into the $Ba_{0.3}In_{0.3}Co_4Sb_{12}$ matrix leads to the dual control of phonons and electrons;[7] the random turning of the magnetic domain for Co-NPs intensifies phonon scattering and concurrently induces multiple scattering of electrons, which allow lower κ and higher S, respectively. Next, the introduction of superparamagnetic Fe_3O_4-NPs into the $Bi_{0.5}Sb_{1.5}Te$ matrix remarkably decreases its κ and significantly increases S *via* enhanced phonon scattering and a dominant carrier multiple scattering mechanism induced by Fe_3O_4-NPs as well.[11] In a similar manner, the synchronized enhancement of the TE properties of Fe- or Co-NP-embedded $MnSi_{1.787}Al_{0.01}$ nanocomposites also points out the importance of the intensified scattering mechanism due to magnetic nanophases.[12] Other than the aforementioned examples, diverse attempts have been made to employ magnetism to enhance TE performance[16] by inducing (para-)magnon-drag,[17–19] magnetic drag,[8,14] electron repository,[20] spin fluctuation,[21] spin entropy[22] and non-saturating Seebeck effects.[23]

In this study, we propose a novel mechanism for amplifying S *via* magnetic-impurity-doping in a host TE material. While previous studies mostly focused on additional scattering induced by the embedded magnetic impurities, our work shows that a doping-induced relaxation of spin polarization near the Fermi level can also contribute to enhancing S and thus achieving a high zT. To demonstrate the concept, we adopt half-metallic higher-manganese silicides (HMSs) doped with the magnetic elements of Fe or Co as a platform. The Fe- or Co-doped HMS polycrystals undergo a decrease in κ and a concurrent increase in $S^2\sigma$, leading to a doubling of zT near 300 K. Spin-polarized density functional theory (DFT) calculations suggest that the magnetic-impurity-doping reduces the total magnetic moment of HMSs accompanying the spin polarization relaxation, which in turn increases the participation of majority-spin carriers in electrical conduction. Such additional participation of majority-spin carriers positively contributes to S following our two-spin-channel model.

Materials and methods

Synthesis of bulk HMS polycrystals

All HMS polycrystals were prepared using a powder metallurgy method. In detail, $MnSi_{1.79}Al_{0.01}$ was selected as the matrix material because of its well-established TE properties and half-metallic nature.[24] The stoichiometric $MnSi_{1.79}Al_{0.01}$ polycrystalline powders were synthesized by the following procedure. First, raw powders of Mn (99.95%, Alfa Aesar), Si (99.9%, Alfa Aesar), and Al (99.5%, Alfa Aesar) were prepared and mixed in a stoichiometric ratio. Then, the powder mixtures were sealed under vacuum in quartz tubes and sintered at 1323 K for 48 h for homogenization. The resulting ingots were ground into powders using high-energy ball milling (8000D, SPEX). For the synthesis of doped samples, the HMS powders were mixed with iron(II) or cobalt(II) acetates ($(CH_3COO)_2Fe$ and $(CH_3COO)_2Co$, respectively) under an Ar atmosphere using a ball mill system to ensure the formation of uniformly distributed Fe or Co elements inside the matrix. Then, the hybrid powders were annealed at 573 K for 2 h under a mixed gas atmosphere (95% N_2 and 5% H_2) to reduce the acetates (–CH_3COO–). The reduced powders were pelletized and sintered using a spark plasma sintering method with the optimized conditions of 1193 K and 60 MPa, which are expected to cause the magnetic-impurity-doping of Fe or Co according to ref. 25. For the undoped (pristine) HMS sample, the same procedure was performed except for the introduction and removal of the acetates. As a result, three different HMS samples including pristine, 1.0 at% of Fe- or Co-doped HMS polycrystals were fabricated with a small amount of undissolved Fe or Co NPs. The detailed microstructure of the HMS samples will be discussed in the following. For comparison, we henceforth label the three samples with their magnetic dopants, *i.e.*, pristine, Fe-HMS and Co-HMS.

Electric and thermoelectric transport property measurements

The synthesized HMS samples were cut into bars, and 8 electrodes were attached to the samples for electric and thermoelectric transport property measurements. In detail, copper and constantan wire electrodes (0.001 in. dia., SPCP/SPCI-001-50, Omega Engineering, Inc.) were attached to side surfaces of each sample using a spot-welding technique. Each wired sample was put on an insulating BeO pad with a silver epoxy adhesive (H20E, EPO-TEK); then, a 120 Ω resistive heater was attached to the top of the sample with the adhesive. Here, the heat sink BeO pad allows quick dissipation of heat from the sample during the heating due to its high thermal conductivity ($\sim$370 W m^{-1} K^{-1}).[26] Then, each assembled sample block was individually mounted on the sample stage of a customized liquid-nitrogen cryostat system (Lake Shore Cryotronics, Inc.) with Apiezon N grease to improve the thermal contact, and the electrodes were soldered to the pins that were electrically

connected to measuring instruments. Next, raw signals of Seebeck voltage, thermal conductivity, and normal and Hall resistances of each sample were monitored under various environmental temperatures from 80 to 300 K. When an electric flux through the sample was given by the two copper wires, one on the top of the sample and one on its bottom, the normal and Hall resistances were output to an AC resistance bridge (model 372, Lake Shore Cryotronics, Inc.) *via* a four-point probe technique. During the Hall resistance measurements, a magnetic field H was swept at about 140 Oe s^{-1}. This process was repeated until the samples had been subjected to all temperatures from 80 to 300 K with increments of 20 K. After the electrical measurements, the resistive heater was turned on to apply heat flux, and then hot temperature T_h, cold temperature T_c and the temperature difference $\Delta T = T_h - T_c$ inside the sample were stabilized within the range of 0.01 K. The T_h, T_c and Seebeck voltages were monitored using a nanovoltmeter (model 2182A, Keithley). All measurements were performed on the sample stage which was kept in a high vacuum ($<10^{-6}$ torr) and covered with a gold-plated radiation shield to avoid unnecessary heat losses during the measurements.

Crystal structure and microstructure characterization

The crystal structures of HMS samples were analyzed by powder X-ray diffraction (XRD) with Cu-Kα radiation for 2θ from 20° to 70° (D/Max-2500, Rigaku). The phase constitutions and lattice parameters of the HMS matrix were estimated using JADE software. The microstructures of HMS samples were examined using secondary electron (SE) imaging and back-scattered electron (BSE) imaging using field emission scanning electron microscopy (FE-SEM) (SU6600, Hitachi) at 15 kV and 29 μA.

Magnetic property measurements

The temperature T and magnetic field H dependences of mass magnetization M were observed using a magnetic property measurement system (MPMS) (Quantum Design, Inc.). In detail, field-cooled magnetization at 0.5 T was monitored in the range of 2 to 300 K and isothermal magnetization was measured at 2 and 300 K in the range from −7 T to 7 T.

Spin-polarized DFT calculations

We studied the $Mn_{15}Si_{26}$ compound by DFT calculations based on the projector augmented wave (PAW) method, which was implemented in the Vienna *ab initio* simulation package (VASP). For the exchange correlation potential, the generalized gradient approximation (GGA) with the Perdew–Burke–Ernzerhof (PBE) was used with a cut-off energy for the plane wave basis set of 500 eV. For the k-mesh, 13 × 13 × 3 centered at the Γ point was used.[27–30] For structural optimization, the energy convergence criteria were set to 10^{-6} eV per f.u. for each electronic step and 10^{-5} eV per f.u. for each ionic step. Here, the unit cell is 4 times the f.u. For the DFT calculations on different total magnetizations, a self-consistent calculation was performed with a rigid band shift at each calculation step. Here, the constrained total magnetization was kept at different values from 0.050 μ_B to 0.067 μ_B per Mn atom, and the constrained calculation was started with the initial spin polarized charge density given by non-constrained calculation. The crystal structures were obtained by structure relaxation, which had an a-axis lattice constant a = 5.491 Å and c-axis lattice constant c = 65.04 Å (Fig. S1 and Table S1 in the ESI†). Based on the electronic structures obtained from the DFT calculations, transport properties such as carrier concentrations were obtained by using the BoltzTraP code.

Results and discussion

Thermoelectric properties

The thermal conductivity κ, electrical conductivity σ, Seebeck coefficient S and TE figure-of-merit zT of all samples were obtained at 80 < T < 300 K (Fig. 1). The κ of Fe-HMS is lower than that of the pristine at all temperatures and gradually increases as T increases. A similar behavior is observed for the κ of Co-HMS, showing a sharper decrease at low T (Fig. 1a). In the meantime, the σ of all samples sharply decreases as T increases (Fig. 1b); this trend demonstrates a typical degenerate-semiconducting or metallic behavior.[31] Each power law exponent of σ slightly changes with the introduction of Fe and Co dopants. Co-HMS has the lowest σ at low T, while it shows the highest σ above the crossover point at ∼200 K. Finally, the S of all samples is positive at all T (Fig. 1c); this result indicates that the samples are p-type semiconductors, and this conclusion is in accordance with the Hall measurement results (Fig. S2 in the ESI†). The pristine has S = 120 μV K^{-1} at 300 K, as reported previously,[32–35] while the introduction of Fe or Co dopants into the HMS polycrystals greatly increases S to 143 μV K^{-1} (19.4% increase) for Fe-HMS and 145 μV K^{-1} for Co-HMS (21.1% increase) at 300 K. Such significant increases of S lead to a doubling of zT in Fe-HMS and Co-HMS at 300 K (Fig. 1d); the decreases in both κ and σ at low T almost compensate each other and thus their changes hardly affect the resulting zT. Therefore, we succeeded in overcoming the counter-indicated nature of TE properties by virtue of the magnetic-impurity-doping. While previous studies attributed the improved TE performance in a similar system to spin-induced additional scattering mechanisms on a qualitative basis, below we attempt to propose a new perspective on the observed enhanced TE performance, including detailed magnetic coupling characteristics.

Microstructures of HMS polycrystals

To understand the underlying mechanisms for the TE properties of our HMS samples (Fig. 1), we first explored their crystal structures and microstructures using XRD, SE and BSE characterization. First, all XRD peaks agree with the standard PDF values (CDS, 20-0724) of the $Mn_{15}Si_{26}$ material (Fig. S3 in the ESI†). These results indicate that the $Mn_{15}Si_{26}$ phase was well formed during the fabrication process. When the Fe or Co dopants are added, the a-axis and c-axis lattice constants of both samples slightly decrease compared to that of the pristine (Table S2 in the ESI†). This observation is consistent with a previous study[25] that the lattice constants of HMS compounds

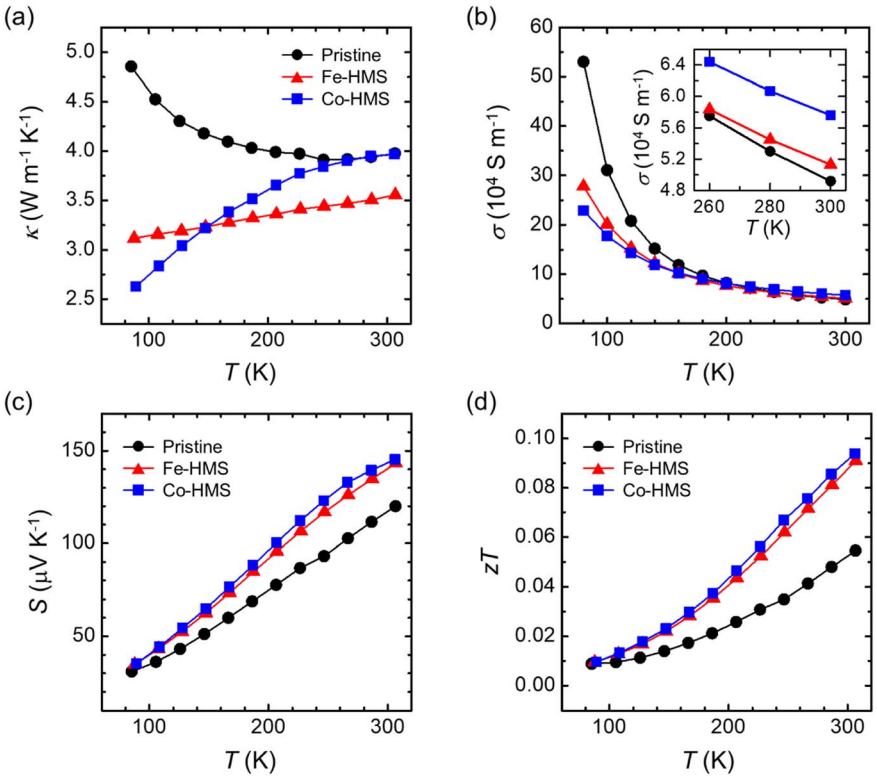

Fig. 1 Temperature T dependence of the (a) thermal conductivity κ, (b) electrical conductivity σ, (c) Seebeck coefficient S and (d) thermoelectric figure-of-merit zT of pristine, Fe-HMS and Co-HMS samples. -●-: Pristine, -▲-: Fe-HMS and -■-: Co-HMS. Inset in (b) shows σ at high temperatures from 260 to 300 K.

$Mn_{1-x}Fe_xSi_{1.73}$ and $Mn_{1-y}Co_ySi_{1.73}$ show a decreasing trend with Fe ($x \leq 0.1$) and Co ($y \leq 0.1$) contents. In ref. 25, it was shown that the a-axis lattice constant decreases from 5.525 Å of $MnSi_{1.73}$ to 5.521 Å for $Mn_{0.98}Fe_{0.02}Si_{1.73}$ and 5.519 Å for $Mn_{0.98}Co_{0.02}Si_{1.73}$. Those values are similar to the estimated a-axis lattice constants of our HMS samples from the XRD analysis, 5.519 Å for Fe-HMS and 5.516 Å for Co-HMS (Table S2 in the ESI†). Considering that the nominal chemical compositions of Fe-HMS and Co-HMS are $Mn_{0.98}Fe_{0.02}Si_{1.75}Al_{0.01}$ and $Mn_{0.98}Co_{0.02}Si_{1.75}Al_{0.01}$, respectively, very close to those in ref. 25, such simultaneous decrease in the a-axis lattice constant suggests that the Fe and Co dopants are successfully substituted into the HMS lattice of our samples. However, several undissolved Fe or Co NPs remain along the grain boundaries of the HMS matrix possibly due to solubility limits (SE and BSE images of Fig. S4 in the ESI†).[12] Therefore, it is concluded that most of the Fe and Co dopants are substitutionally dissolved in the HMS lattice with several residues distributed along the grain boundaries. Here, we assume that the amount of the residues is negligibly small and almost no secondary phases exist inside the HMS matrix judging from the XRD results.

Magnetic properties

How Fe and Co dopants are magnetically coupled over the HMS matrix can be reliably detected by measuring the magnetic properties of HMS polycrystals, including the temperature dependence of magnetization (M–T) and the magnetic-field dependence of magnetization (M–H) (Fig. 2a–c). All the HMS polycrystals exhibit ferromagnetic ordering below the Curie temperature of about 50 K (Fig. 2a); the M abruptly increases as the T decreases due to a paramagnetic to ferromagnetic transition below the Curie temperature. In detail, the M of Fe-HMS and Co-HMS at 2 K (ferromagnetic phase), far lower than the Curie temperature, is 0.143 emu g^{-1} and 0.091 emu g^{-1}, respectively, much lower than that of the pristine sample (0.313 emu g^{-1} at 2 K). In addition, the magnetic transition temperature slightly shifts to lower temperatures when the magnetic dopants are added. This change in the magnetic behavior is also observed in M–H plots at 2 K (Fig. 2b); the M of the pristine sample at 7 T is about 0.472 emu g^{-1} while Fe-HMS and Co-HMS have nearly half that of the pristine. This implies that the magnetic doping may induce antiferromagnetic coupling between the magnetic dopants and Mn ions in the HMS polycrystals, which will be discussed in detail later. However, the M–H plots at 300 K (Fig. 2c) suggest that part of Fe and Co NPs remain undissolved in the HMS matrix, giving rise to the observed ferromagnetic behavior in the low field regime (inset of Fig. 2c). Particularly, the M of Co-HMS at 1 T is 0.005 emu g^{-1} while that of Fe-HMS at 1 T is 0.013 emu g^{-1}, almost twice that of Co-HMS. Given that a pure Fe metal has 28% higher magnetic moment than a pure Co metal[36,37] and ultrafine Fe particles also have been reported to have 52% higher saturation magnetization than Co particles,[38] it is reasonable that Fe-HMS shows relatively strong ferromagnetic behavior compared to Co-HMS.

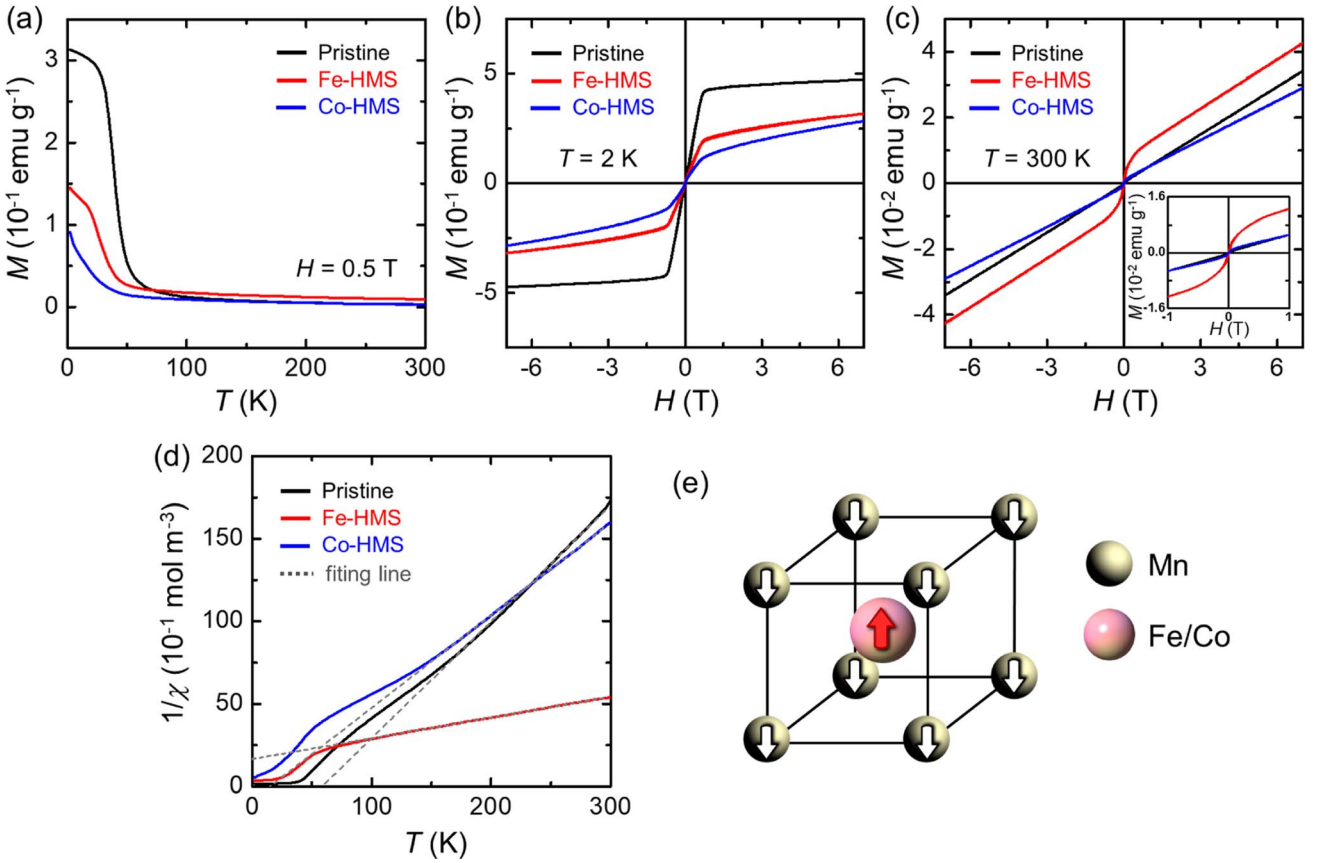

Fig. 2 Magnetic properties of HMS polycrystals. (a) Mass magnetization M *versus* temperature T (M–T) plots and (b and c) mass magnetization M *versus* magnetic field H (M–H) plots for HMS polycrystals at (b) 2 K and (c) 300 K. Inset in (c) shows low-field M measurements. (d) The measured temperature T dependence of the inverse of magnetic susceptibility $1/\chi$. The grey dashed lines are fitting lines for the prediction of the Curie–Weiss constant of each sample. (e) A schematic description of the magnetic structure of the doped HMS polycrystals.

Moreover, this ferromagnetic behavior in the low field is also in accordance with a previous study,[12] in which the magnetic NPs are locally dispersed near the grain boundaries without being diffused into the bulk HMS lattice.

To examine in depth the magnetic structure of the HMS polycrystals, we observed changes in their inverse of magnetic susceptibility $1/\chi$ with temperature T. By extrapolating and fitting the temperature dependence of $1/\chi$ of the three HMS samples with the Curie–Weiss law (Fig. 2d), we can estimate their Curie–Weiss constants of 58.5 K in the pristine, −132.1 K in Fe-HMS and 14.9 K in Co-HMS; here, the Curie–Weiss constant of the pristine is similar to a previously reported value.[39] Such decreases in the Curie–Weiss constants *via* magnetic doping imply that the doped Fe or Co ions weaken the intrinsic ferromagnetic order of Mn ions. The detailed magnetic structure can be better understood by examining the saturation magnetic moment p_{sat} and the effective magnetic moment p_{eff}; p_{sat} is the maximum magnetic moment while p_{eff} is the root-mean-square of the magnitudes of individual local magnetic moments excluding long-range magnetic ordering. The former can be calculated from the saturation magnetization M_s of each sample and the latter can be obtained by fitting experimental $1/\chi$ plotted against T following the Curie–Weiss law of $1/\chi = \frac{T - T_c}{N p_{eff}^2 \mu_B}$ (T_c: Curie temperature, N: Avogadro constant and μ_B: Bohr magneton).[40] As summarized in Table 1, the p_{sat} at 2 K considerably decreases from 9.43×10^{-3} μ_B per Mn of the pristine to 6.32×10^{-3} μ_B per Mn of Fe-HMS and 5.67×10^{-3} μ_B per Mn of Co-HMS. In contrast, the p_{eff} reaches 8.41×10^{-1} μ_B per Mn in Fe-HMS and 3.98×10^{-1} μ_B per Mn in Co-HMS; both are higher than 3.55×10^{-1} μ_B per Mn of the pristine. Considering the high-spin Fe^{2+} and Co^{2+} moments (5.4 μ_B on Fe^{2+} and 4.8 μ_B on Co^{2+})[31] compared to the weak total magnetic moment of the HMS system (0.067 μ_B per Mn), such significant reduction of p_{sat} in the doped samples suggests that the Fe/Co dopants and Mn ions are antiferromagnetically coupled with each other as schematically shown in Fig. 2e. As for the p_{eff}, the presence of ferromagnetic Fe and Co nano-precipitates in the

Table 1 (a) Saturation magnetic moment p_{sat} at 2 K and (b) effective magnetic moment p_{eff} of HMS polycrystals

	p_{sat} (μ_B per Mn)	p_{eff} (μ_B per Mn)
Pristine	9.43×10^{-3}	3.55×10^{-1}
Fe-HMS	6.32×10^{-3}	8.41×10^{-1}
Co-HMS	5.67×10^{-3}	3.98×10^{-1}

HMS matrix could lead to the larger p_{eff} values in the doped samples as mentioned above. The relatively strong increase of p_{eff} in Fe-HMS could be due to a larger concentration of undissolved nano-precipitates in the matrix. Based on the above observations, we can now describe the magnetic structure of our HMS polycrystals. Intrinsically, the HMS has a spiral spin structure of Mn ions along the *c*-axis, forming an itinerant weak ferromagnet.[39,40] Introducing strong magnetic dopants such as Fe or Co into the lattice breaks such magnetic order by causing antiferromagnetic coupling, while undissolved Fe or Co NPs contribute their large magnetic moments to increasing local magnetic moments.

From the perspective of transport properties, such alteration of magnetic structures due to the magnetic-impurity-doping can induce a significant effect. The occurrence of antiferromagnetic coupling can cause shifts in band structures in order to balance the exchange splitting energy between spin-polarized bands. Therefore, below we will delve into such a perspective in more detail and show that the changes in spin-polarized band structures caused by the magnetic-impurity-doping indeed profoundly affect the transport behaviors of our HMS system.

Spin-polarized band structures of HMS samples

We will first investigate how the magnetic-impurity-doping alters the band structure in detail. Since the experimental temperature range is from 80 to 300 K which is much higher than the Curie temperature of the HMS (~50 K), we will assume that the band structure is in the fluctuating local band regime where the spin-polarized electron spectral functions still exist due to the local magnetic moments. In this regime, the long-range order is broken and suppressed due to scattering events, responsible for spin-mixing; however, the short-range magnetic order remains alive and the Stoner mechanism, one of the widely accepted models to describe the long-range order in itinerant ferromagnets, can still work for locally describing the band structure even in the paramagnetic state above the Curie temperature.[41,42] Thus, the spin-polarized DFT calculations of the $Mn_{15}Si_{26}$ phase in the ground state at 0 K are expected to successfully describe its electronic structure even above the Curie temperature and help to understand in more detail how the above-mentioned antiferromagnetic coupling alters the electronic transport.

As shown in Fig. 3a, the spin-polarized DFT calculations show that $Mn_{15}Si_{26}$ has a half-metallic ground state with only minority-spin (or down-spin) bands at the Fermi level. The half-metallicity could originate from the strong Hund's rule energy stabilization,[43] which aligns unpaired spins of itinerant electrons near the Fermi level in the same direction as many as possible; here, the unpaired spins exist when the number of unoccupied states in the valence band near the Fermi level is small. In addition, such alignment of low-concentrated spins

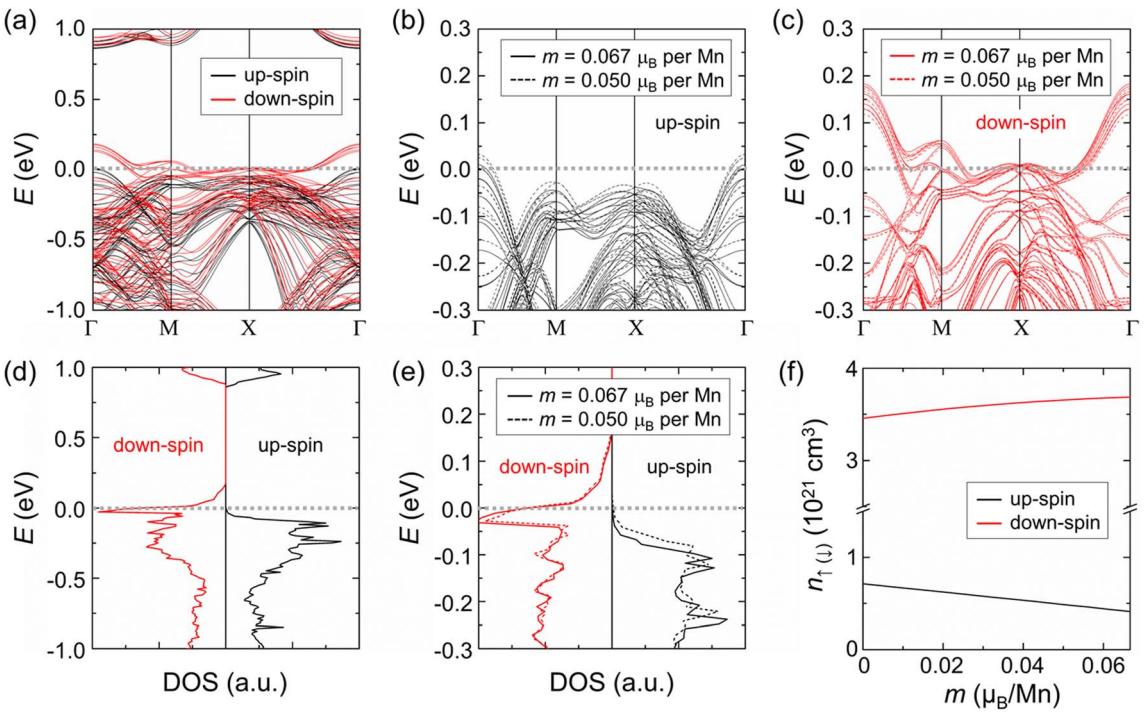

Fig. 3 Spin-polarized density functional theory (DFT) calculation results of the $Mn_{15}Si_{26}$ phase. (a) The spin-dependent band structures of $Mn_{15}Si_{26}$. The black and red solid lines correspond to the up-spin and down-spin bands, respectively, and the grey dashed line at $E = 0$ represents the Fermi level. Comparison of (b) up-spin and (c) down-spin band structures in the low energy regime between the pristine ($m = 0.067\ \mu_B$ per Mn) and magnetically doped ($m = 0.050\ \mu_B$ per Mn) cases. The solid and dotted lines correspond to the magnetic moment $m = 0.067\ \mu_B$ per Mn and $m = 0.050\ \mu_B$ per Mn, respectively. (d) Density-of-states (DOS) of up- and down-spin bands of pristine $Mn_{15}Si_{26}$. (e) Comparison of the up-spin and down-spin DOS in the low energy regime between the pristine and magnetically doped cases. (f) Magnetic moment *m* dependence of the carrier concentration $n_{\uparrow(\downarrow)}$ of up(down)-spin bands of the HMS material.

contributes to weak ferromagnetic behavior of the HMS. The calculated magnetic moment for each Mn atom is 0.067 μ_B on average, which ensures a low spin density of 4 electrons per unit cell. To be more specific, unequally distributed magnetic moments of Mn atoms range from 0 to 0.3 μ_B throughout the unit cell.

In addition, it is clearly seen that both up- and down-spin bands have similar quadratic band dispersions near the Fermi level at the Γ point. In general, band dispersions in itinerant ferromagnets are known to differ between the two spin components when the ferromagnets have large local magnetic moments ($\sim$ a few μ_B per atom);[44] however, our HMS material has much smaller local magnetic moments and thus the resulting band dispersions are not much dependent on the spin polarization. These observations allow us to assume the same density-of-states (DOS) effective mass for both up- and down-spin bands, which helps to simplify our two-spin-channel model as discussed later.

Due to such a characteristic of spin polarization, the transport properties of our HMS samples should be explained by considering both electron channels of up- and down-spin bands. For example, for the case of the pristine, the top of up-spin bands is located slightly below the Fermi level, while that of the down-spin bands crosses the Fermi level leading to a half-metallic DOS, and thus the carrier transport is dominated by only down-spin electrons. However, the magnetic-impurity-doping of Fe or Co can drastically alter the magnetic structure as previously discussed, and in turn, the transport properties. In detail, when the strong magnetic ions are doped in a weak ferromagnetic metal such as HMSs, Ruderman–Kittel–Kasuya–Yosida (RKKY)-type exchanges between the Fe/Co dopants and Mn ions in the HMS lattice, which antiferromagnetically couples the localized spins of Fe/Co dopants and the itinerant spins of nearby conduction electrons, can occur due to the Friedel oscillation generated by the localized spins of the doped Fe/Co ions, which leads to the reduction of total magnetic ordering.[45] As a result, the up(down)-spin bands near the Fermi level move upward (downward) to balance the magnetic ordering of electronic states; since the total number of localized electrons is considered to be constant due to the low doping concentration, the decrement of occupied up-spin states is supposed to be equal to the increment of occupied down-spin states. To closely examine such a correlation between the magnetic moment changes and band shifts of the HMS system, we calculated spin-dependent band structures for the pristine and magnetically doped cases by decreasing the total magnetic moment m from 0.067 μ_B per Mn to 0.050 μ_B per Mn (Fig. S5 in the ESI†); here, the value of 0.067 μ_B per Mn corresponds to the calculated total magnetic moment of $Mn_{15}Si_{26}$ and is slightly larger than 9.43×10^{-3} μ_B per Mn, the experimentally measured value for the pristine. It is because the polycrystalline ferromagnets generally have magnetic disorders such as anti-phase boundaries,[46] whose presence could reduce the total magnetic moment to a certain extent.

As shown in Fig. 3b and c, the decreased magnetic ordering makes the up(down)-spin bands move upward (downward), but the magnitude of shift of the down-spin bands is negligibly small compared to that of the up-spin bands. This difference in the degree of band shifts arises from the difference in the DOS of each band near the Fermi level; the down-spin bands possess a large DOS near the Fermi level, but the up-spin bands have almost zero DOS near the Fermi level (Fig. 3d). Thus, a much larger upward shift of the DOS of up-spin bands occurs with the decrease of magnetic moment than the downward shift of the DOS of down-spin bands (Fig. 3e). In other words, although the pristine is half-metallic and the spins of electrons at the Fermi level are fully polarized with down-spins only, the magnetic-impurity-doping can decrease the magnitude of the spin polarization as a result of the involvement of the up-spin bands near the Fermi level. Here, we call this phenomenon as the "spin polarization relaxation."

The relaxed spin polarization induced by antiferromagnetic coupling can have profound effects on the transport properties, by altering the relative participation of two spin-polarized electrons in transport. As shown in Fig. 3f, when the calculated magnetic moment m decreases from 0.067 μ_B per Mn of the pristine down to the value of 0.050 μ_B per Mn, the number of itinerant up-spin electrons monotonically increases whereas that of down-spin electrons slowly decreases; specifically, the slope of the curve for the up-spin electrons is negative over the whole range of m, while the instantaneous slope of the curve for the down-spin electrons is approximately flat at an m of 0.067 μ_B per Mn, which gradually becomes positive with the decrease of m. As a consequence, the up-spin electrons in the magnetically doped cases have a much larger impact on transport compared to those in the pristine, while the total carrier concentration, the sum of carrier concentrations of each band, remains almost the same (or slightly increases) as that of the pristine. In short, the spin polarization relaxation induced by the reduction of magnetic ordering upon the magnetic doping introduces additional up-spin electron contribution to the carrier transport in the HMS system.

Based on the above description, we will hereafter focus on identifying the underlying mechanism for the strong TE performance enhancement in the Fe-HMS and Co-HMS samples, by carefully examining how the antiferromagnetic-coupling-mediated changes in the spin-dependent band structures affect the carrier transport and the resultant TE properties.

Discussion on the thermoelectric properties

First, the decreases in κ as a result of the magnetic-impurity-doping of Fe and Co are also observed in the lattice thermal conductivity κ_L, obtained by subtracting the electronic contribution from κ using the Wiedemann–Franz law of $\kappa_{elec} = L\sigma T$ (κ_{elec}: electron thermal conductivity and L: the Lorentz number) (Fig. S6 in the ESI†); both Fe-HMS and Co-HMS show decreasing κ_L as T decreases. These results are opposite to that of the pristine, of which both κ and κ_L increase as T decreases, resembling the intrinsic phonon thermal conductivity due to Umklapp scattering.[47] Such reduction in the κ and κ_L of Fe-HMS and Co-HMS at low T could be attributed to additional phonon scattering mechanisms such as atomic point defect

scattering[48,49] due to the magnetic dopants in the lattice with the help of nanoprecipitate scattering[50–52] due to residual NPs along the grain boundaries.

Second, for the case of σ, given the conventional law of $\sigma = ne\mu$ (n: carrier concentration, e: elementary charge and μ: carrier mobility),[47] σ relies on the changes in n and μ which can be estimated from $n = 1/eR_H$ and $\mu = \sigma R_H$ (R_H: Hall coefficient), respectively, with the assumption of a single parabolic band.[31] The n of our HMS samples is almost constant regardless of temperature (Fig. 4a), a typical behavior of degenerately doped semiconductors.[53] The n averaged over the measured T of the magnetic-ion-doped HMS samples is 1.91×10^{21} cm^{-3} in Fe-HMS and 2.34×10^{21} cm^{-3} in Co-HMS; those values are a bit larger than that of the pristine (1.59×10^{21} cm^{-3}). This slight increase in n could be due to the spin polarization relaxation upon magnetic doping as discussed previously, while the hole (h^+) transfer from Fe and Co NPs to the HMS medium could also contribute to the increase of n according to metal–semiconductor contact theory.[12] Next, the μ of our HMS samples rapidly decreases as T rises (Fig. 4b) and thus mainly determines the T dependence of σ. Such a negative slope is a signature of phonon-electron scattering, and the power law dependence of μ on T provides the exponents of -1.62 for the pristine, -1.29 for Fe-HMS and -1.11 for Co-HMS. It is known that the carrier mobility due to acoustic phonon scattering follows the $\sim T^{-3/2}$ law in semiconductors.[54] Several previous studies have observed the $\sim T^{-3/2}$ dependence of Hall mobility in undoped HMSs.[55–57] Therefore, the exponent values estimated above suggest that the acoustic phonon scattering is the major electron scattering mechanism in our HMS samples. The larger exponents in the doped samples are possibly due to the presence of additional scattering mechanisms such as ionized impurity scattering and multiple carrier scattering at the interface between the host and nano-precipitates.[7,12,54] Furthermore, μ has a value of 1.66 cm^2 V^{-1} s^{-1} in Fe-HMS and 1.53 cm^2 V^{-1} s^{-1} in Co-HMS at 300 K; those values are similar to that of pristine (1.86 cm^2 V^{-1} s^{-1} at 300 K). This similarity in μ between the HMS samples at higher T, combined with the slightly increased n by the Fe/Co doping, leads to the observed crossover between the σ of the three samples near $\sim$200 K (Fig. 1b).

Finally, we develop a two-spin-channel model for the analysis of S in our magnetic-impurity-doped HMS samples. This analysis is based on the spin-dependent band structures estimated from the spin-polarized DFT calculations. The two-spin-channel model overcomes the shortcomings of the conventional single parabolic band model, by taking into account the effect of the magnetic structure on the transport properties. We find from the subsequent analysis results that the increase of S originates from a decrease in the ferromagnetic order of the HMS matrix as a result of the magnetic-impurity-doping and the subsequent increase in the participation of majority (up)-spin currents in transport.

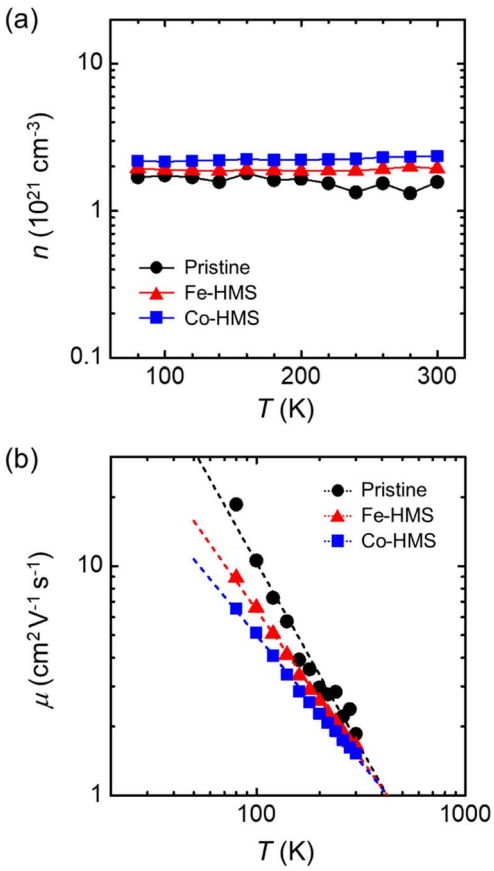

Fig. 4 Temperature T dependence of (a) total carrier concentration n and (b) carrier mobility μ of pristine, Fe-HMS and Co-HMS samples. -●-: pristine, -▲-: Fe-HMS and -■-: Co-HMS. The dashed lines are fitting lines for the prediction of the power law exponents.

Two-spin-channel model analysis of the Seebeck coefficient

As discussed in the previous sections, the HMS is an itinerant ferromagnet, where majority-spin electrons and minority-spin electrons have each conduction channel. Therefore, the two current channels are expected to independently affect the TE properties, specifically S; in such a two-spin-channel scheme, the total Seebeck coefficient S_{tot} from both channels is weighted by the corresponding electrical conductivities such that[58–60]

$$S_{tot} = \frac{\sigma_\uparrow S_\uparrow + \sigma_\downarrow S_\downarrow}{\sigma_\uparrow + \sigma_\downarrow} \quad (1)$$

where $\sigma_{\uparrow(\downarrow)}$ and $S_{\uparrow(\downarrow)}$ denote the electrical conductivity and the Seebeck coefficient of the up(down)-spin channel, respectively. To thoroughly investigate the role of each term in eqn (1), the expressions for $\sigma_{\uparrow(\downarrow)}$[61] and $S_{\uparrow(\downarrow)}$[4] are given by

$$\sigma_{\uparrow(\downarrow)} = \frac{n_{\uparrow(\downarrow)} e^2 \tau_{\uparrow(\downarrow)}}{m_D^*} \quad (2)$$

$$S_{\uparrow(\downarrow)} = \frac{2\pi^{2/3}}{3^{5/3}} \frac{{k_B}^2}{e\hbar^2} T \left(\frac{3}{2} + \lambda_{\uparrow(\downarrow)}\right) \frac{m_D^*}{{n_{\uparrow(\downarrow)}}^{2/3}} \quad (3)$$

taken at the Fermi level E_F for a degenerate semiconductor ($E_F \gg k_B T$, k_B: Boltzmann constant) with a parabolic band and a single type of carrier. Here, $\hbar$ is the reduced Planck constant and m_D^* is the DOS effective mass, while $n_{\uparrow(\downarrow)}$, $\tau_{\uparrow(\downarrow)}$ and $\lambda_{\uparrow(\downarrow)}$ are

the carrier concentration, the scattering relaxation time, and the scattering parameter of the up(down)-spin channel, respectively. In our analysis, m_D^* can be considered as spin-independent, since the band dispersions of both spin channels from the DFT calculation results are very similar to each other as mentioned above. In addition, it is assumed that $\tau_{\uparrow(\downarrow)}$, $\lambda_{\uparrow(\downarrow)}$ and m_D^* are independent of temperature for simplification. As a result of combining eqn (1)–(3), we can express S_{tot} in terms of the two electronic channels such that

$$S_{tot} = \frac{2\pi^{2/3}}{3^{5/3}} \frac{{k_B}^2}{e\hbar^2} m_D^* T \frac{\left(\frac{3}{2}+\lambda_\uparrow\right)\tau_\uparrow {n_\uparrow}^{1/3} + \left(\frac{3}{2}+\lambda_\downarrow\right)\tau_\downarrow {n_\downarrow}^{1/3}}{\tau_\uparrow n_\uparrow + \tau_\downarrow n_\downarrow} \quad (4)$$

which depends on the scattering-related parameters of $\tau_{\uparrow(\downarrow)}$ and $\lambda_{\uparrow(\downarrow)}$ and the carrier concentration of each channel of $n_{\uparrow(\downarrow)}$. Evaluating S_{tot} is challenging since it requires the estimation of m_D^*, $\tau_{\uparrow(\downarrow)}$, $\lambda_{\uparrow(\downarrow)}$ and $n_{\uparrow(\downarrow)}$. We can first estimate m_D^* by considering the relatively simple band dispersion of the pristine, where only down-spin bands cross the E_F. For simplicity, we further assume that those down-spin bands can be represented by a single parabolic dispersion, based on the similarity between them. The Seebeck coefficient of pristine S_0 can then be defined using eqn (3) considering $\lambda_\downarrow$ and $n_\downarrow$ only:

$$S_0 = \frac{2\pi^{2/3}}{3^{5/3}} \frac{{k_B}^2}{e\hbar^2} T\left(\frac{3}{2}+\lambda_\downarrow\right) \frac{m_D^*}{{n_\downarrow}^{2/3}} \quad (5)$$

With the temperature-independent n and $\lambda_\downarrow \sim -1/2$ for the dominant acoustic phonon scattering in the pristine, we can obtain m_D^* of the pristine by linearly fitting the T dependence of experimental S_0 data. Our experimental fit to the measured S_0 for the pristine gives an m_D^* of 7.685 m_0 (m_0: electron mass), which is comparable to previously reported values (Fig. S7 in the ESI†).[62,63] As discussed earlier, similar dispersions of the down- and up-spin bands near the E_F in all three samples warrant identical m_D^*. Now that we have the estimated m_D^* of 7.685 m_0 for all three HMS samples, we can hereafter explain the underlying mechanism for the enhanced S in Fe-HMS and Co-HMS considering $\tau_{\uparrow(\downarrow)}$, $\lambda_{\uparrow(\downarrow)}$, and $n_{\uparrow(\downarrow)}$ in eqn (4). We will first discuss electron scattering and then investigate an important aspect of carrier concentration.

According to the previously obtained power law exponents of carrier mobility, acoustic phonon scattering is the dominant electron scattering mechanism in all three HMS samples, while ionized impurity scattering and multiple carrier scattering at the interface between the host and nano-precipitates could make additional contributions in Fe-HMS and Co-HMS. Since λ for acoustic phonon scattering is in general spin-independent, we can set both scattering parameters for up-spin $\lambda_\uparrow$ and down-spin $\lambda_\downarrow$ equal to a single spin-independent scattering parameter λ. Accordingly, the scattering relaxation times of each band $\tau_\uparrow$ and $\tau_\downarrow$ in eqn (4) are estimated to be nearly the same following the relation $\tau = \tau_0 E^\lambda$ (τ: scattering relaxation time, τ_0: energy-independent scaling coefficient, E: energy, and λ: scattering parameter),[64] which holds for solids with parabolic bands. Therefore, eqn (4) can be simplified as follows:

$$S_{tot} = \frac{2\pi^{2/3}}{3^{5/3}} \frac{{k_B}^2}{e\hbar^2} m_D^* T\left(\frac{3}{2}+\lambda\right) \frac{{n_\uparrow}^{1/3} + {n_\downarrow}^{1/3}}{n} \quad (6)$$

The effect of carrier concentration on S_{tot} can be evaluated by carefully observing $n_\uparrow$ and $n_\downarrow$ in eqn (6). As described earlier, the change in $n_{\uparrow(\downarrow)}$ is directly related to the spin-dependent band shifts, so it can be inspected by analyzing the spin-resolved band structure of the HMS materials; near the E_F, the pristine has only down-spin bands, whereas Fe-HMS and Co-HMS experience the doping-induced upward shifts of up-spin bands with nearly fixed down-spin bands. That being said, the $n_\downarrow$ values of all samples are supposed to be comparable irrespective of the presence of magnetic impurities, while $n_\uparrow$ noticeably increases as a result of the magnetic-impurity-doping in Fe-HMS and Co-HMS. Consequently, the $n_\uparrow$ of all samples can be calculated by subtracting the measured n of the pristine (equivalent to $n_\downarrow$ for all samples) from those of Fe-HMS or Co-HMS (Table 2). Here, we use n averaged over the measured T for each sample based on its negligible temperature dependence. Then, using the estimated $n_{\uparrow(\downarrow)}$ and measured n of each sample with the conditions that $\lambda = -1/2$ and $m_D^* = 7.685\ m_0$ as evaluated earlier, we can estimate the S_{tot} of Fe-HMS and Co-HMS with eqn (6) and compare them with the measured values of S. As shown in Fig. 5, the estimated S_{tot} agrees well with the measured S. Meanwhile, the single parabolic band (SPB) approximation has been popularly used for examining the change in S due to its simplicity. The SPB model can be represented without the weighing factors of two-spin bands as follows:

$$S = \frac{2\pi^{2/3}}{3^{5/3}} \frac{{k_B}^2}{e\hbar^2} T\left(\frac{3}{2}+\lambda\right) \frac{m_D^*}{n^{2/3}} \quad (7)$$

With the average n over T of Fe-HMS and Co-HMS, an m_D^* of 7.685 m_0 and the dominant acoustic phonon scattering ($\lambda = -1/2$), we can also estimate the T dependent S for each sample with eqn (7) (Fig. 5). However, it is noted that there are significant disagreements between the measured S of Fe-HMS and Co-HMS and the estimated S with the SPB model. In fact, the estimated S with the SPB model rather explain well the measured S of the pristine. This seems reasonable because in the pristine only down-spin bands with parabolic dispersions near the E_F contribute to S. Since the $n_\downarrow$ values of all three samples are comparable, we can infer from eqn (6) that the observed strong enhancement in the S of Fe-HMS and Co-HMS is attributed to the participation of $n_\uparrow$ induced by the magnetic-impurity-doping. The proposed two-spin-channel model, as demonstrated in this example, enables a detailed spin-resolved

Table 2 The change in the averaged carrier concentration $n_{\uparrow(\downarrow)}$ of up(down)-spin bands of our HMS samples

	$n_\uparrow$ (cm^{-3})	$n_\downarrow$ (cm^{-3})
Pristine	—	1.59×10^{21}
Fe-HMS	3.20×10^{20}	1.59×10^{21}
Co-HMS	6.58×10^{20}	1.59×10^{21}

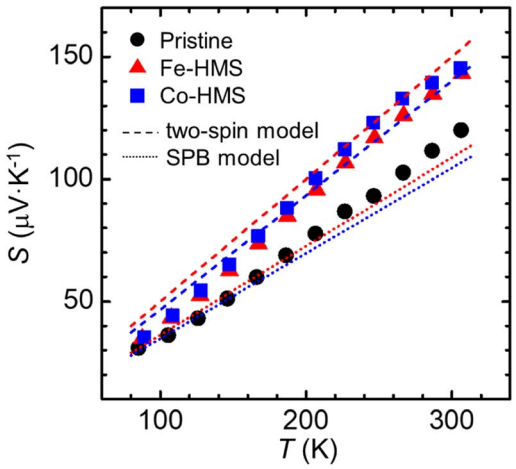

Fig. 5 The comparison between the measured and estimated Seebeck coefficient S of Fe-HMS and Co-HMS. The red (Fe-HMS) and blue (Co-HMS) dashed lines correspond to the estimated S from the two-spin-channel model and the dotted lines correspond to the estimated S from the single parabolic band (SPB) model. ●: Pristine, ▲: Fe-HMS and ■: Co-HMS. (T: temperature).

analysis of experimentally measured transport data, which is hardly captured by the SPB model.

The novel interpretation for the enhanced S in the magnetic-impurity-doped HMS described thus far can be briefly summarized with a general contour plot of the normalized Seebeck coefficient S_{norm} as a function of magnetic moment m and carrier concentration n (Fig. 6). Here, we calculated n using the BoltzTraP code in the spin-polarized DFT calculations, while S_{norm} was estimated from a simplified form of eqn (6) without the factor of $\frac{2\pi^{2/3}}{3^{5/3}}\frac{{k_B}^2}{e\hbar^2}m_D^* T$ to demonstrate a general concept. Under the same conditions of dominant acoustic phonon scattering as above, it is obvious that the change in m significantly affects S, especially near the half-metal line (the diagonal line in Fig. 6), which stands for 100% spin polarization. For example, when it comes to conventional TE materials with zero magnetic moment, S increases as n decreases (the horizontal arrow in Fig. 6) following the Mott relation.[65] However, once the magnetic ordering is involved, the change in m can play a pivotal role in determining S. Especially near the half-metal line, decreasing m for a fixed n leads to a large increase in S (the vertical arrow in Fig. 6). The underlying mechanism is identical to that described above: the reduced m indicates a relaxed spin polarization, which induces additional participation of up-spin electrons ($n_\uparrow$) in transport. Seemingly, the addition of $n_\uparrow$ should increase n, but since $n_\uparrow$ is smaller than $n_\downarrow$ or n by one order (Table 2), n can be assumed to be nearly constant upon reducing m by magnetic doping. Thus, we can conclude that in a spin-polarized system such as half-metals, manipulating m is an effective way to enhance S. As one approach, we have demonstrated that introducing magnetic-impurity-dopants that antiferromagnetically couple to host ions effectively reduces m for a given n, leading to significantly enhanced S.

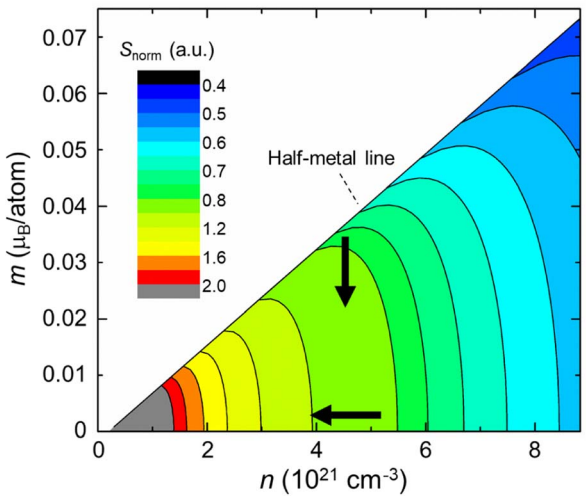

Fig. 6 A contour plot of the normalized Seebeck coefficient S_{norm} as a function of the magnetic moment m and the carrier concentration n. Here, the white region corresponds to the impossible area where the band structures cannot be predicted due to the limit of n.

Conclusions

We propose a novel mechanism to greatly increase the Seebeck coefficient by exploiting the spin-polarized band structure of magnetic TE materials, without compromising the thermal conductivity and electrical conductivity. In detail, by doping strong magnetic Fe/Co ions into the half-metallic HMS material, we successfully demonstrate ~20% enhancement of the Seebeck coefficient leading to a doubling of zT at 300 K. According to magnetic susceptibility measurements, the magnetic-impurity-doping induces an RKKY-type antiferromagnetic ordering in the HMS matrix. Spin-polarized DFT calculations reveal that such antiferromagnetic ordering induces relaxation of the spin-polarized bands. As a result, in the doped samples, up-spin electrons start to participate in transport in addition to down-spin electrons, whereas only down-spin electrons contribute to transport in the pristine sample. Through two-spin-channel analysis, we show that such additional contribution of up-spin electrons is the key to explaining the observed large enhancement of S in the doped samples.

Our study provides a novel perspective regarding the Seebeck coefficient enhancement recently observed in various magnetic systems. We show that manipulating magnetization in a way that induces the relaxation of spin polarization of the band structure can significantly increase the Seebeck coefficient. Such manipulation could be realized simply by introducing magnetic impurity dopants into a host TE material. Admittedly, we do not exclude the possibility that other mechanisms such as spin-mediated scattering could be at work independently or in combination with the proposed mechanism, depending on the system of interest. We believe that the spin polarization relaxation *via* the introduction of antiferromagnetic coupling between host magnetic ions and magnetic impurities can be utilized as a general strategy to enhance the Seebeck coefficient

in magnetic systems, which opens up many possibilities in magnetism-mediated TE materials. In future research, not only half metallic systems such as spinel ferrites ($FeCr_2O_4$ and VFe_2O_4),[66–68] but nonmagnetic semiconductors doped with magnetic impurities, such as $Cr_xSb_{2-x}Te_3$,[69] $Fe_xBi_{2-x}Te_3$ [70] and $Fe_x(Bi, Sb)_{2-x}Te_3$ [71] which possess weak ferromagnetism and a low carrier concentration, could be promising systems to implement the proposed strategy.

Conflicts of interest

There are no conflicts to declare.

Acknowledgements

This work was supported by the National Research Foundation of Korea (NRF) Grant funded by the Korea government (NRF-2020R1C1C1004291, NRF-2020K1A4A7A02095438 and NRF-2022M3C1A3091988). This work was supported by the Basic Science Research Program through the National Research Foundation of Korea (NRF) funded by the Ministry of Education, Korea government (2020R1F1A1052898 and 2021R1A2C2010972) and Ministry of Science and ICT, Korea Government (2020R1A5A1019141).

References

1 B. Poudel, Q. Hao, Y. Ma, Y. Lan, A. Minnich, B. Yu, X. Yan, D. Wang, A. Muto, D. Vashaee, X. Chen, J. Liu, M. S. Dresselhaus, G. Chen and Z. Ren, *Science*, 2008, **320**, 634–638.
2 D. Wu, L.-D. Zhao, S. Hao, Q. Jiang, F. Zheng, J. W. Doak, H. Wu, H. Chi, Y. Gelbstein, C. Uher, C. Wolverton, M. Kanatzidis and J. He, *J. Am. Chem. Soc.*, 2014, **136**, 11412–11419.
3 W. Li, L. Zheng, B. Ge, S. Lin, X. Zhang, Z. Chen, Y. Chang and Y. Pei, *Adv. Mater.*, 2017, **29**, 1605887.
4 H. Jin and J. P. Heremans, *Phys. Rev. Mater.*, 2018, **2**, 115401.
5 G. A. Slack, *CRC Handbook of Thermoelectrics*, CRC Press, Boca Raton, FL, USA, 1995.
6 M. S. Dresselhaus, G. Chen, M. Y. Tang, R. G. Yang, H. Lee, D. Z. Wang, Z. F. Ren, J.-P. Fleurial and P. Gogna, *Adv. Mater.*, 2007, **19**, 1043–1053.
7 W. Zhao, Z. Liu, Z. Sun, Q. Zhang, P. Wei, X. Mu, H. Zhou, C. Li, S. Ma, D. He, P. Ji, W. Zhu, X. Nie, X. Su, X. Tang, B. Shen, X. Dong, J. Yang, Y. Liu and J. Shi, *Nature*, 2017, **549**, 247–251.
8 J. B. Vaney, S. Aminorroaya Yamini, H. Takaki, K. Kobayashi, N. Kobayashi and T. Mori, *Mater. Today Phys.*, 2019, **9**, 100090.
9 L. Zhao, C. Chen, L. Pan, X. Hu, C. Lu and Y. Wang, *J. Appl. Phys.*, 2019, **125**, 095107.
10 S. Chandra, P. Dutta and K. Biswas, *ACS Appl. Energy Mater.*, 2020, **3**, 9051–9057.
11 C. Li, S. Ma, P. Wei, W. Zhu, X. Nie, X. Sang, Z. Sun, Q. Zhang and W. Zhao, *Energy Environ. Sci.*, 2020, **13**, 535–544.
12 G. Kim, H.-S. Kim, H. S. Lee, J. Kim, K. H. Lee, J. W. Roh and W. Lee, *Nano Energy*, 2020, **72**, 104698.
13 Y. Zhao, X. Nie, C. Sun, Y. Chen, S. Ke, C. Li, W. Zhu, X. Sang, W. Zhao and Q. Zhang, *ACS Appl. Mater. Interfaces*, 2021, **13**, 58746–58753.
14 R. Fortulan, S. Aminorroaya Yamini, C. Nwanebu, S. Li, T. Baba, M. J. Reece and T. Mori, *ACS Appl. Energy Mater.*, 2022, **5**, 3845–3853.
15 X. Wu, Z. Wang, Y. Liu, X. Sun, Y. Xu, Y. Tian, B. Wang, X. Sang, J. Shi and R. Xiong, *J. Alloys Compd.*, 2022, **904**, 163933.
16 F. H. Sun, S. F. Ma, W. Y. Zhao, C. C. Li, X. H. Sang, P. Wei and Q. J. Zhang, *Rep. Prog. Phys.*, 2021, **84**, 096501.
17 M. V. Costache, G. Bridoux, I. Neumann and S. O. Valenzuela, *Nat. Mater.*, 2012, **11**, 199–202.
18 Y. Zheng, T. Lu, M. M. H. Polash, M. Rasoulianboroujeni, N. Liu, M. E. Manley, Y. Deng, P. J. Sun, X. L. Chen, R. P. Hermann, D. Vashaee, J. P. Heremans and H. Zhao, *Sci. Adv.*, 2019, **5**, eaat9461.
19 R. Ang, A. U. Khan, N. Tsujii, K. Takai, R. Nakamura and T. Mori, *Angew. Chem.*, 2015, **54**, 12909–12913.
20 W. Zhao, Z. Liu, P. Wei, Q. Zhang, W. Zhu, X. Su, X. Tang, J. Yang, Y. Liu, J. Shi, Y. Chao, S. Lin and Y. Pei, *Nat. Nanotechnol.*, 2017, **12**, 55–60.
21 N. Tsujii, A. Nishide, J. Hayakawa and T. Mori, *Sci. Adv.*, 2019, **5**, eaat5935.
22 P. Sun, K. R. Kumar, M. Lyu, Z. Wang, J. Xiang and W. Zhang, *Innovation*, 2021, **2**, 100101.
23 B. Skinner and L. Fu, *Sci. Adv.*, 2018, **4**, eaat2621.
24 H. Lee, G. Kim, B. Lee, K. H. Lee and W. Lee, *J. Electron. Mater.*, 2017, **46**, 3242–3248.
25 T. Itoh and S. Uebayashi, *J. Jpn. Soc. Powder Powder Metall.*, 2016, **63**, 491–496.
26 G. A. Slack and S. B. Austerman, *J. Appl. Phys.*, 1971, **42**, 4713–4717.
27 G. Kresse and J. Hafner, *Phys. Rev. B: Condens. Matter Mater. Phys.*, 1993, **47**, 558–561.
28 P. E. Blöchl, *Phys. Rev. B: Condens. Matter Mater. Phys.*, 1994, **50**, 17953–17979.
29 G. Kresse and J. Furthmüller, *Phys. Rev. B: Condens. Matter Mater. Phys.*, 1996, **54**, 11169–11186.
30 G. Kresse and D. Joubert, *Phys. Rev. B: Condens. Matter Mater. Phys.*, 1999, **59**, 1758–1775.
31 N. W. Ashcroft and N. D. Mermin, *Solid State Physics*, Cengage Learning, Belmont, CA, USA, 1976.
32 A. S. Orekhov, V. V. Klechkovskaya, E. V. Rakova, F. Y. Solomkin, S. V. Novikov, L. V. Bochkov and G. N. Isachenko, *Semiconductors*, 2017, **51**, 887–890.
33 Z. Li, J.-F. Dong, F.-H. Sun, S. Hirono and J.-F. Li, *Chem. Mater.*, 2017, **29**, 7378–7389.
34 Z. Li, J.-F. Dong, F.-H. Sun, Asfandiyar, Y. Pan, S.-F. Wang, Q. Wang, D. Zhang, L. Zhao and J.-F. Li, *Adv. Sci.*, 2018, **5**, 1800626.
35 S. Ghodke, A. Yamamoto, H.-C. Hu, S. Nishino, T. Matsunaga, D. Byeon, H. Ikuta and T. Takeuchi, *ACS Appl. Mater. Interfaces*, 2019, **11**, 31169–31175.
36 L. Pauling, *Phys. Rev.*, 1938, **54**, 899–904.

37 B. Balke, S. Wurmehl, G. H. Fecher, C. Felser and J. Kübler, *Sci. Technol. Adv. Mater.*, 2008, **9**, 014102.
38 W. Gong, H. Li, Z. Zhao and J. Chen, *J. Appl. Phys.*, 1991, **69**, 5119–5121.
39 U. Gottlieb, A. Sulpice, B. Lambert-Andron and O. Laborde, *J. Alloys Compd.*, 2003, **361**, 13–18.
40 T. Nakajima and J. Schelten, *J. Magn. Magn. Mater.*, 1980, **21**, 157–166.
41 V. Korenman, J. L. Murray and R. E. Prange, *Phys. Rev. B: Condens. Matter Mater. Phys.*, 1977, **16**, 4032–4047.
42 D. W. Jeong, H. C. Choi, C. H. Kim, S. H. Chang, C. H. Sohn, H. J. Park, T. D. Kang, D.-Y. Cho, S. H. Baek, C. B. Eom, J. H. Shim, J. Yu, K. W. Kim, S. J. Moon and T. W. Noh, *Phys. Rev. Lett.*, 2013, **110**, 247202.
43 T. Saitoh, M. Nakatake, A. Kakizaki, H. Nakajima, O. Morimoto, S. Xu, Y. Moritomo, N. Hamada and Y. Aiura, *Phys. Rev. B: Condens. Matter Mater. Phys.*, 2002, **66**, 035112.
44 T. Herrmann and W. Nolting, *J. Phys.: Condens. Matter*, 1999, **11**, 89–107.
45 M. A. Ruderman and C. Kittel, *Phys. Rev.*, 1954, **96**, 99–102.
46 D. T. Margulies, F. T. Parker, M. L. Rudee, F. E. Spada, J. N. Chapman, P. R. Aitchison and A. E. Berkowitz, *Phys. Rev. Lett.*, 1997, **79**, 5162–5165.
47 A. C. Beer, *Solid State Physics, Suppl. 4: Galvanomagnetic Effects in Semiconductors*, Academic Press, New York, NY, USA, 1963.
48 P. G. Klemens, *Proc. Phys. Soc. A*, 1955, **68**, 1113–1128.
49 J. Callaway and H. C. von Baeyer, *Phys. Rev.*, 1960, **120**, 1149–1154.
50 A. Majumdar, *J. Heat Transfer*, 1993, **115**, 7–16.
51 W. Kim and A. Majumdar, *J. Appl. Phys.*, 2006, **99**, 084306.
52 M. Y. Kim, S. J. Park, G.-Y. Kim, S.-Y. Choi and H. Jin, *Energy Environ. Sci.*, 2021, **14**, 3480–3491.
53 G. Tan, L.-D. Zhao and M. G. Kanatzidis, *Chem. Rev.*, 2016, **116**, 12123–12149.
54 M. Dresselhaus, G. Dresselhaus, S. B. Cronin and A. G. S. Filho, *Solid State Properties: from Bulk to Nano*, Springer, Berlin, Germany, 2018.
55 X. Chen, A. Weathers, D. Salta, L. Zhang, J. Zhou, J. B. Goodenough and L. Shi, *J. Appl. Phys.*, 2013, **114**, 173705.
56 X. She, X. Su, H. Du, T. Liang, G. Zheng, Y. Yan, R. Akram, C. Uher and X. Tang, *J. Mater. Chem. C*, 2015, **3**, 12116–12122.
57 V. Ponnambalam and D. T. Morelli, *Mater. Res. Express*, 2019, **6**, 025507.
58 H. J. Xiang and D. J. Singh, *Phys. Rev. B: Condens. Matter Mater. Phys.*, 2007, **76**, 195111.
59 S. Sharma and S. K. Pandey, *Phys. Lett. A*, 2015, **379**, 2357–2361.
60 A. S. Botana, P. M. Botta, C. de la Calle, A. Piñeiro, V. Pardo, D. Baldomir and J. A. Alonso, *Phys. Rev. B: Condens. Matter Mater. Phys.*, 2011, **83**, 184420.
61 J. P. Heremans, C. M. Thrush and D. T. Morelli, *J. Appl. Phys.*, 2005, **98**, 063703.
62 Y. Sadia, Z. Aminov, D. Mogilyansky and Y. Gelbstein, *Intermetallics*, 2016, **68**, 71–77.
63 W.-D. Liu, Z.-G. Chen and J. Zou, *Adv. Energy Mater.*, 2018, **8**, 1800056.
64 J. P. Heremans, C. M. Thrush and D. T. Morelli, *Phys. Rev. B: Condens. Matter Mater. Phys.*, 2004, **70**, 115334.
65 N. F. Mott and E. A. Davis, *Electronic Processes in Non-crystalline Materials*, Oxford University Press, New York, NY, USA, 1979.
66 M. H. N. Assadi, J. J. Gutiérrez Moreno and M. Fronzi, *ACS Appl. Energy Mater.*, 2020, **3**, 5666–5674.
67 J. Nell and B. J. Wood, *Am. Mineral.*, 1991, **76**, 405–426.
68 J. A. G. Cerón, D. A. L. Téllez and J. Roa-Rojas, *J. Electron. Mater.*, 2022, **51**, 822–830.
69 P. M. Tarasov, V. A. Kulbachinskii and V. G. Kytin, *J. Exp. Theor. Phys.*, 2007, **105**, 21–26.
70 V. A. Kulbachinskii, A. Y. Kaminskii, K. Kindo, Y. Narumi, K. Suga, P. Lostak and P. Svanda, *Phys. B*, 2002, **311**, 292–297.
71 J. Pei, J. Dong, B. Cai, Y. Zhang, W. Zhou, B.-P. Zhang, Z.-H. Ge and J.-F. Li, *Mater. Today Phys.*, 2021, **19**, 100423.

